Contralateral-Ipsilateral Segregation as a Conserved Principle of the Visual Corpus Callosum

Jiaowen Wang [a, #], Yanming Wang [b, #], Yiping An [c, #], Shishuo Chen [b, #], Huan Wang [d], Benedictor Alexander Nguchu [e, f], Muhammad Mohsin Pathan [b], Yueyi Yu [b], Sinan Yang [b], Ying-Qiu Zheng [g], Yang Ji [b], Hao Wang [c, *], Yifeng Zhou [a, *], Bensheng Qiu [b, *], Xiaoxiao Wang [b, *]

[a] Hefei National Laboratory for Physical Sciences at the Microscale, School of Life Sciences, University of Science and Technology of China, Hefei, China.

[b] Medical Imaging Center, Department of Electronic Engineering and Information Science, University of Science and Technology of China, Hefei, China

[c] MoE Key Laboratory of Brain-inspired Intelligent Perception and Cognition, Anhui Province Key Laboratory of Biomedical Imaging and Intelligent Processing, HFCNS Institute of Artificial Intelligence, National Engineering Laboratory for Brain-inspired Intelligence Technology and Application, School of Information Science and Technology, University of Science and Technology of China, Hefei, 230026, China

[d] State Key Laboratory of Brain and Cognitive Science, Institute of Biophysics, Chinese Academy of Sciences, Beijing 100101, China.

[e] Oujiang Laboratory (Zhejiang Lab for Regenerative Medicine, Vision and Brain Health), Wenzhou Medical University, Wenzhou, Zhejiang, China

[f] School of Ophthalmology and Optometry and Eye Hospital, Wenzhou Medical University, Wenzhou, Zhejiang, China

[g] Wellcome Centre for Integrative Neuroimaging, FMRIB, Nuffield Department of Clinical Neurosciences, Oxford, UK

# These authors contribute equally to the work.
* Corresponding:
haowang@ustc.edu.cn, zhouy@ustc.edu.cn, bqiu@ustc.edu.cn, wang506@ustc.edu.cn

Abstract:

How the corpus callosum (CC) integrates the left and right visual fields to create a unified perceptual experience is a fundamental unresolved question. It remains unresolved whether the CC transmits this information via segregated parallel channels or through mixed, integrated pathways. Here, we resolve this by creating a multimodal functional blueprint of the forceps major (FMA), the principal component of the visual callosum, in humans and mice. By combining ultra-high-field 7T fMRI with Bayesian population receptive field (pRF) modeling in humans, we directly test the competing hypotheses: segregated streams should manifest as voxels dominated by single pRFs, whereas integrated signals would produce voxels with multiple pRFs. Our results reveal a functionally segregated architecture dominated by single pRFs (expected probability 0.92), forming parallel streams that represent the contralateral (87.7%) and distinct ipsilateral (12.3%) visual field. In contrast, integrative dual pRFs are sparse and localized to the cortical boundary, reflecting the localized convergence of bilateral axons. This organizational principle is anatomically corroborated at the mesoscale in the mouse, where dual-color neuronal viral tracing and whole-brain light sheet microscopy imaging reveal a complementary laminar segregation of callosal fibers. Collectively, these findings establish that the visual callosum operates as a set of parallel, segregated information conduits, providing a new framework for understanding unified visual perception and for investigating callosal disruptions in neurological disorders.

Keywords: corpus callosum, forceps major, Bayesian population receptive field, viral tracing, fiber tract tracing, visual cortex, interhemispheric communication

1. Introduction

The corpus callosum (CC), a deeply conserved structure across mammals (Gavrish et al., 2024; Suárez et al., 2018), integrates information between the brain's two hemispheres to create a unified perceptual experience (Gazzaniga, 2000; Schulte & Müller-Oehring, 2010). Within the visual system, the CC tracts fuse inputs from the contralateral visual cortices (Wandell et al., 2007) into a single, coherent perception (Bocci et al., 2014; Rivest et al., 1994). Our study focuses on the forceps major (FMA), the largest component of the visual callosum (Goldstein et al., 2025), where a central, unresolved question remains: is visual information transmitted via segregated parallel streams or mixed?

The "segregated" hypothesis predicts that hemispheric callosal tracts are clustered and segregated from the tracts from another hemisphere, and therefore a singular voxel in Magnetic Resonance Imaging (MRI) predominantly carries information from a single visual hemifield. In contrast, a "mixed" model would suggest that bihemispheric tracts are mixed, thus individual voxels receive and pool inputs from both hemifields. Adjudicating between these models is critical, as a segregated architecture would permit the decoding of directional information flow directly from functional MRI (fMRI) signals. This allows researchers to move beyond mapping anatomical links (Chung et al., 2024; H. Huang et al., 2024; Santana et al., 2023) — "who is connected" — to decoding directional information flow — "who is talking to whom".

A fundamental principle of neural wiring is that axons maintain the topographic information of their source regions: visual callosal connections, for instance, exhibit a visuotopic organization mirroring their cortical origins (Rochefort et al., 2009; Sincich & Blasdel, 2001). Historically, testing this principle within white matter has been challenging. However, recent advances have demonstrated that reliable fMRI signals can be detected in white matter (Ding et al., 2018; Fraser et al., 2012; Y. Huang et al., 2023; Ji et al., 2023; Zhao et al., 2023) and visuotopic organization is preserved within these tracts (H. Wang et al., 2023; Y. Wang et al., 2024). This methodological convergence allows the "segregated versus mixed" question to be reframed as a directly testable hypothesis: a "segregated" architecture predicts voxels dominated by single pRFs, whereas an "mixed" architecture predicts voxels with multiple pRFs.

To directly test this hypothesis, we employ a multi-modal, cross-species investigation. In humans, we combine ultra-high-field 7T fMRI (Benson et al., 2018) with Bayesian population receptive field (pRF) modeling (Zeidman et al., 2018) to map the functional topology, and use diffusion tractography (F. C. Yeh et al., 2013; F.-C. Yeh et al., 2018) to delineate its anatomical substrate. For mesoscale validation, we employ dual-color neuronal viral tracing and whole brain light-sheet microscopic imaging (Ma et al., 2023; H. Wang et al., 2019) in mice to reveal the underlying circuit architecture. This multi-modal approach allows us to construct the comprehensive functional blueprint of the primary interhemispheric visual pathway.

2. Results

Bayesian pRF Modeling Reveals Distinct Receptive Field Topologies in FMA

To directly arbitrate between the segregation and integration hypotheses of callosal function, we applied Bayesian pRF modeling to ultra-high-field 7T fMRI signals from the FMA. A formal model comparison decisively favored a segregated architecture: the single pRF model, which posits that callosal voxels carry information from one visual hemifield, was overwhelmingly dominant (expected probability = 0.92), whereas models assuming integration (dual or triple pRFs) received minimal support (Fig. 1A). Voxels best explained by the single pRF model were distributed throughout the core of the FMA fiber bundle. In contrast, the sparse population of integrative dual pRF voxels clustered near the occipital gray-white matter interface (Fig. 1B), suggesting proximity to cortical regions enhances bilateral integration. The pRF models robustly captured the Blood Oxygenation Level Dependent (BOLD) signal variance (Fig. 1C, 1D), confirming the high fidelity of our functional data.

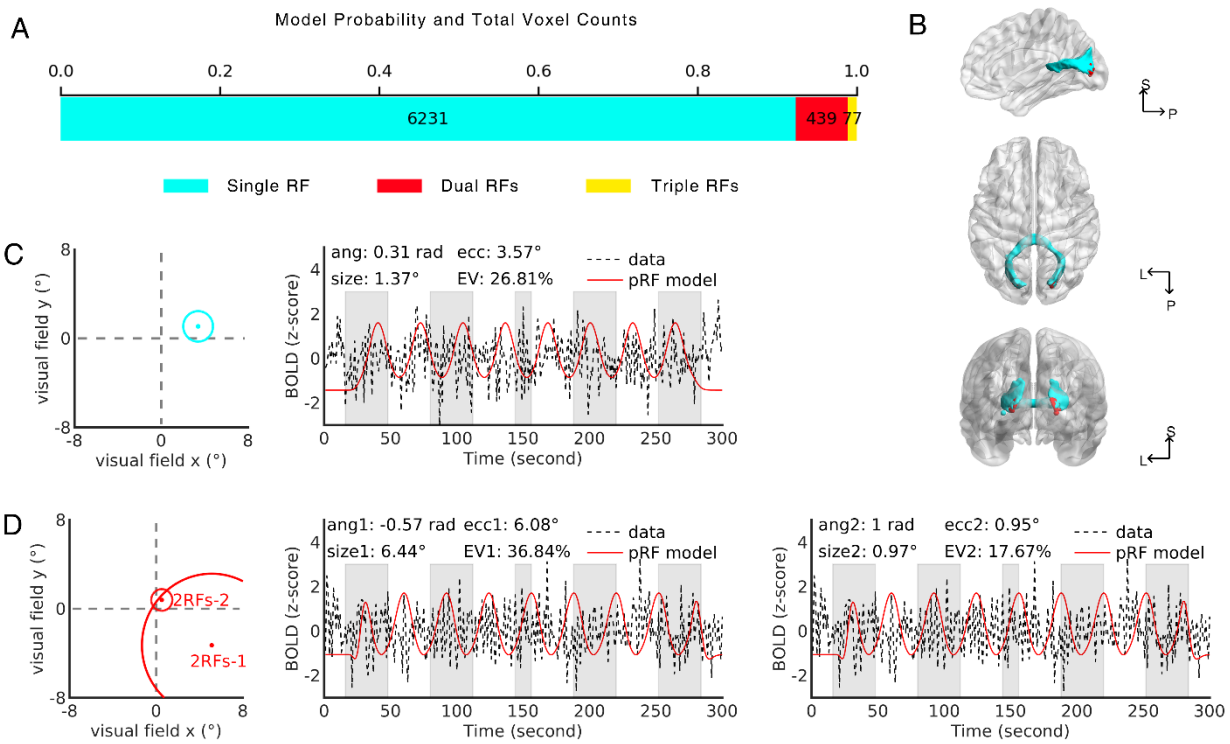

Figure 1. Visual Mapping in FMA Based on Single, Dual, and Triple Receptive Field Models Across All Thresholded Voxels. (A) The expected probability of each model under cross-voxel comparison. Blue, red, and yellow represent the single, dual, and triple receptive fields in the pRF model, respectively. (B) Distribution patterns of the single receptive field model and dual receptive field model on axial and sagittal views. Blue and red colors represent the winning voxels for the single and dual pRF models, respectively. (C, D) In the left panel, the dot indicates the center of the pRF, and the circle represents its size. The right panel shows the distance unit in degrees of visual angle (dva). EV refers to the explained variance from the fMRI time series fitting, where black dashed lines represent the known time series data and red solid lines represent the fMRI-predicted sequences of pRF under the given stimuli. The blue and red represent the corresponding example voxels under single and dual pRF models, respectively.

Parallel Contralateral–Ipsilateral Organization of the FMA

Retinotopic mapping of the dominant single pRFs revealed a novel parallel functional architecture within the FMA, as visualized in Fig. 2A. The polar angle maps (Fig. 2A, angle columns), where red/orange tones represent the right visual field and cyan/blue the left, confirm the expected contralateral organization (87.7% of voxels), with the FMA in each hemisphere displaying the opposing color. Critically, however, we identified distinct and spatially coherent streams of the ipsilateral color (12.3%) running parallel to the main contralateral tracts. This parallel contralateral-ipsilateral organization establishes a previously unknown information channel within the human visual callosum. The validity of this unique parallel information flow was further confirmed by an independent gradient-based analysis, which yielded a convergent result (Fig. 2B). Projection of the FMA gradient analysis onto the visual cortex (Supplementary Fig. S1) confirmed the canonical contralateral organization of vision, with the left hemisphere representing the right visual field and the right hemisphere representing the left, consistent with prior findings.

The functional properties of these streams were further characterized by their retinotopic parameters. Eccentricity maps (Fig. 2A, eccentricity columns), where warmer colors like yellow and red denote greater distance from the fovea, demonstrate that the FMA preferentially represents the para-foveal and peripheral visual fields while excluding the central 0.5° fovea. Consistent with cortical organization, the population receptive fields in the FMA are large, and their size scales linearly with eccentricity (Fig. 2A, size columns). The high Explained Variance (EV) values across the FMA validate the robustness of these findings, confirming that our pRF models reliably capture the highly structured retinotopic information present in the white matter BOLD signal (Fig. 2A, EV columns). Similarly, dorsal callosal pathways exhibit a retinotopic organization analogous to the FMA, characterized by a dominance of single, contralateral-preferring receptive fields alongside a distinct ipsilateral representation (Supplementary Fig. S2).

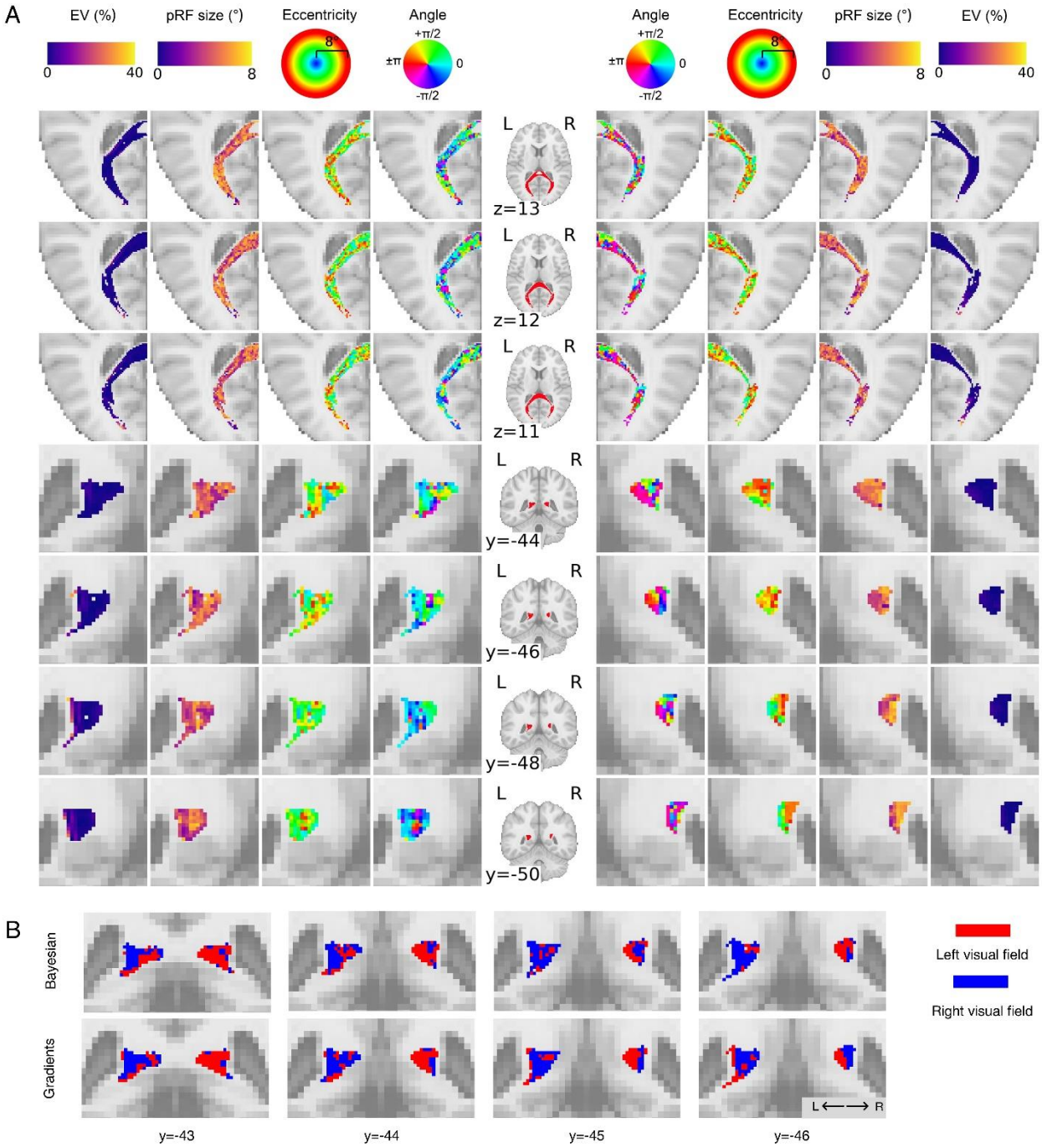

Figure 2. Population receptive field (pRF) parameter maps in the forceps major (FMA). (A) Population receptive field (pRF) parameter maps for the winning single pRF model, shown in selected axial (top rows) and coronal (bottom rows) views. From the center outwards, columns display the FMA mask, polar angle, eccentricity, pRF size, and explained variance (EV). The polar angle maps (where red/orange tones represent the right visual field and cyan/blue the left) reveal a clear parallel organization of dominant contralateral streams alongside smaller, distinct ipsilateral streams. Eccentricity and pRF size maps further characterize these streams, showing a preferential representation of the visual periphery with large receptive fields. (B) Independent validation of the angular organization in a representative coronal slice. The Bayesian pRF model estimate (top) and a

functional gradient analysis (bottom) both reveal the same parallel retinotopic structure, with red and blue indicating representations of the right and left visual fields, respectively. All maps are overlaid on the ICBM 152 2009c standard brain template.

Further pRF analysis revealed a consistent retinotopic organization in FMA mirroring that of the visual cortex (Supplementary Fig. S3A). Eccentricity maps showed that the FMA preferentially represents the para-foveal and peripheral visual fields (Supplementary Fig. S3B), with a notable exclusion of the central 0.5° fovea (Supplementary Fig. S3C). As expected, pRF size scaled linearly with eccentricity (R^2=0.24, p<0.001; Supplementary Fig. S3D). The hemodynamic responses in the FMA were delayed and prolonged compared to gray matter (peak latency: 8.81 s vs. 5.00 s, Supplementary Fig. S3E), consistent with known white matter physiology (M. Li et al., 2019). The robustness of these findings was affirmed by split-half reliability tests, which revealed high consistency of pRF parameter estimates across independent data subsets (e.g., polar angle ICC=0.4538; Supplementary Fig. S4). Analysis of these dual pRF-dominated voxels revealed heterogeneous yet highly structured tuning patterns. The majority exhibited bilateral visual field selectivity, responding to stimuli in both the contralateral and ipsilateral hemifields, with receptive fields often clustered near the horizontal meridian (Supplementary Fig. S5A). Critically, even within these integrative voxels, a strong contralateral bias was evident: contralateral pRFs explained significantly more variance than their ipsilateral counterparts in both the left (17.95±0.85% vs. 4.98±0.33%, $p < 0.001$) and right hemispheres (16.87±0.60% vs. 4.82±0.24%, $p < 0.001$) (Supplementary Fig. S5B). Furthermore, even when dual pRFs shared a contralateral alignment, their receptive fields remained spatially separate (Supplementary Fig. S5C, D). Together, these findings characterize callosal integration as a localized and specialized function that retains a strong contralateral dominance, reinforcing the overarching theme of functional segregation.

Fiber Tractography Delineates the Anatomical Substrate of Functional Streams

To delineate the anatomical substrates of the functionally-defined visual field representations within the FMA, we employed a deterministic fiber tracking approach at the group level (F. C. Yeh et al., 2013). Using the functionally defined contralateral and ipsilateral representations as seeds, we reconstructed the associated white matter pathways. This function-to-structure mapping revealed two anatomically distinct, parallel fiber bundles traversing the FMA (Fig. 3A&B). The tracts corresponding to the left (pink) and right (blue) visual fields maintained a clear topographical separation throughout their trajectory (Fig. 3C&D). This clear topographical organization of axonal projections provides a structural correlate for the retinotopic maps observed in our functional analysis, supporting a model of functional segregation mediated by anatomically discrete pathways.

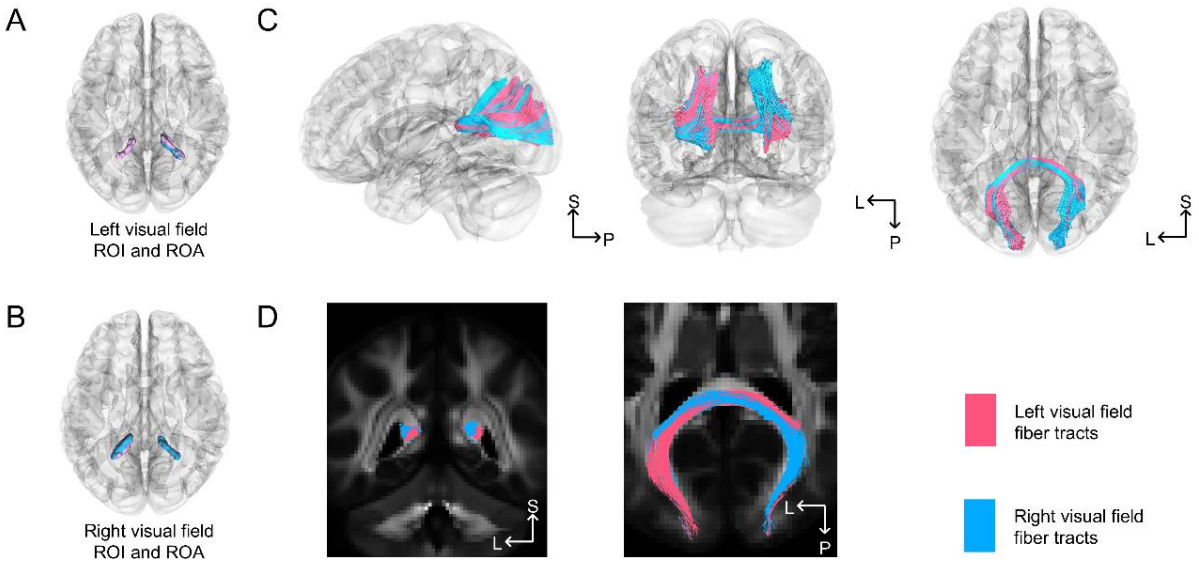

Figure 3. **Deterministic fiber tracking results demonstrating parallel information projection in the forceps major (FMA).** (A) Regions used for deterministic tractography in the left visual field condition. Pink indicates the region of interest (ROI), and blue indicates the region of avoidance (ROA). (B) Regions used for deterministic tractography in the right visual field condition. Blue indicates the ROI, and pink indicates the ROA. (C) Reconstructed fiber bundles visualized in sagittal, coronal, and axial views in Montreal Neurological Institute (MNI) space. (D) Coronal and axial slices highlighting the central portions of the fiber bundles for improved structural delineation. Pink denotes fibers associated with the left visual field, and blue denotes fibers associated with the right visual field.

Anatomical and Mesostructural Evidence for Segregated Pathways

To further validate our findings with a higher resolution, we applied dual-color neuronal viral tracing and light sheet microscopy imaging on whole mouse brain to visualize the organization of two hemispheric fiber tracts at corpus callosum (Fig. 4A). We selectively labeled callosal projections from each hemisphere with adeno-associated viruses (AAV) expressing EGFP and tdTomato injected into the right and left V1 regions, respectively. Utilizing tissue clearing and VISoR light-sheet microscopy, we acquired dual-channel fluorescence images of viral labeled fiber tracts and an extra autofluorescence channel for brain structure at micrometer resolution for whole mouse brain. Viral labeling of visual fiber tracts was confirmed by confined injection loci in V1 (Fig. 4B-C). Our observations revealed that the viral labeled V1 axons projected to the contralateral hemisphere, recapitulating findings in human brain. Dual-color viral labeling revealed that axonal bundles crossing the corpus callosum underwent a transient positional inversion, with their relative dorsal-ventral orientations swapped within the commissural tract. This inverted configuration was maintained over a defined segment of the callosal pathway, after which the bundles resumed a parallel trajectory and ultimately occupied spatially segregated positions in the contralateral hemisphere (Fig. 4D-E). Additionally, volumetric analysis revealed partial but significant spatial segregation between the two fiber tracts located bilaterally external to the midline of the corpus callosum (Dice = 0.15 - 0.38, Jaccard = 0.08 - 0.24), indicating that they projected in parallel while remaining only partially

overlapping. (Fig. 4F-G, Supplementary Fig. S6A-G).

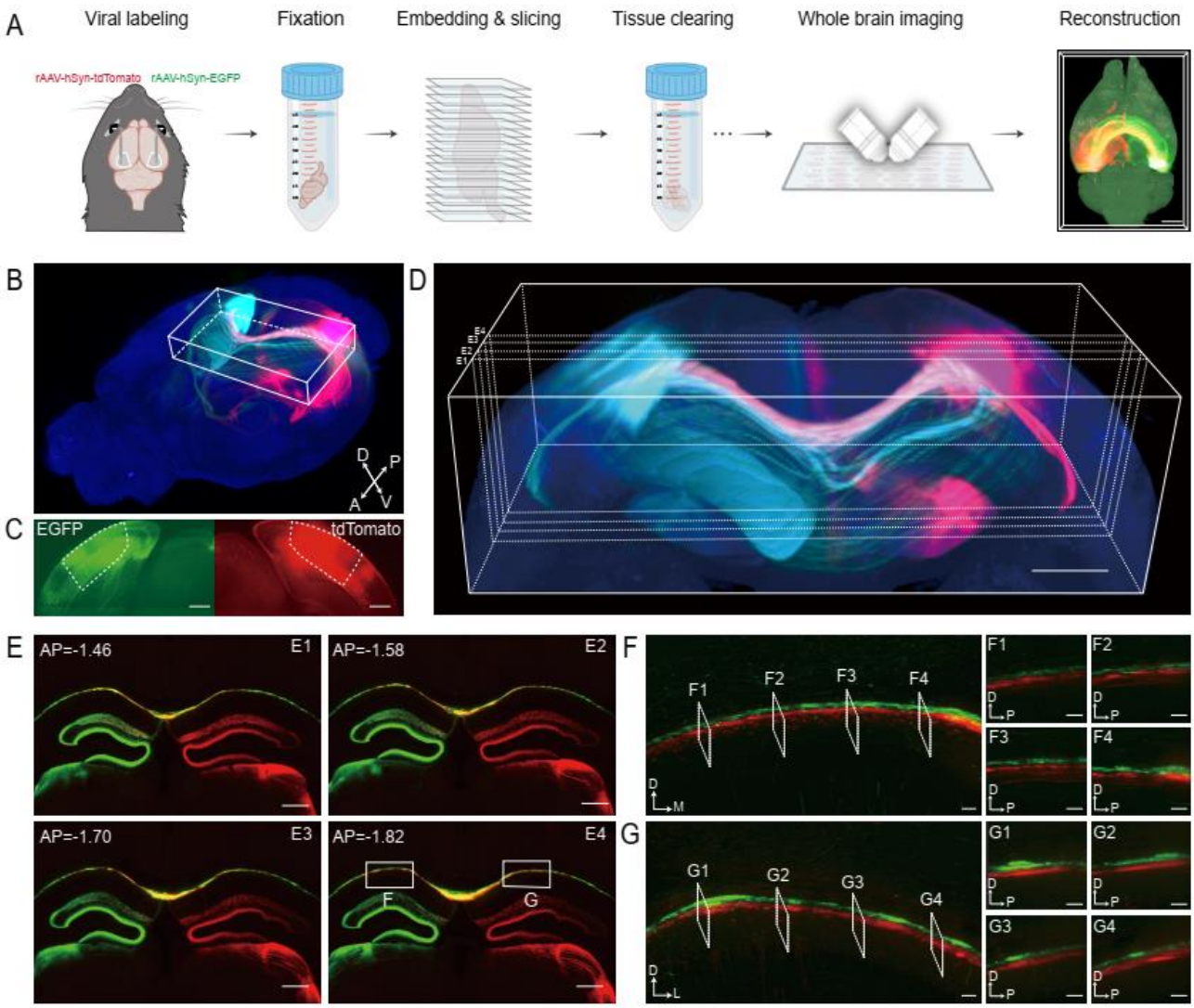

Figure 4. Organization of interhemispheric visual cortical projections revealed by dual-color viral tracing. (A) Pipeline of whole brain viral labeling and imaging: viral labeling, brain fixation with transcardial perfusion, brain embedding and slicing, tissue clearing, whole-brain imaging and 3D reconstruction. Scale bar: 1 mm. (B) Three-dimensional reconstruction and visualization of the axonal projections expressing rAAV-hSyn-EGFP (green) and rAAV-hSyn-tdTomato (red) in the whole brain. A: anterior; P: posterior; D: dorsal; V: ventral. (C) Virus injection and expression is confined in two V1 regions respectively. Scale bar: 300 μm. (D) The ROI showing axonal projections in the CC, with a volume of 3950 × 1440 × 1970 μm^3. Scale bar: 500 μm. (E) Maximum intensity projections of coronal CC sections were generated from 20-μm-thick image stacks. Scale bar: 500 μm. AP: anterior-posterior. (F&G) Structural features of the corpus callosum, with ROIs outlined in white. (F1-F4) & (G1-G4) Representative sagittal sections through the corresponding ROIs along the medial-lateral axis, spaced at 200 μm intervals. Scale bars: 50 μm.

3. Discussion

This study establishes that the visual CC is governed by a conserved principle of contralateral-ipsilateral segregation. Our multi-modal evidence provides a comprehensive validation of this principle. In humans, functional mapping demonstrated that callosal channels are dominated by inputs from a single hemifield, a finding corroborated by both pRF modeling and functional gradient analysis (Fig. 2B) and aligned with discrete anatomical tracts (Fig. 3). We then confirmed the conserved nature of this organization at the mesoanatomical level in mice, where dual-color viral tracing revealed a novel, non-overlapping laminar arrangement of axons from the contralateral and ipsilateral hemispheres (Fig. 4). These convergent findings reveal that the visual CC operates as a set of parallel, segregated conduits, preserving the distinction between information streams originating from the two sides of the visual field.

From Human Function to Mesoscale Anatomy

A central challenge in neuroscience is to bridge the macro- and meso-scales of brain connectivity, by integrating human non-invasive imaging with animal-based invasive tracing techniques (Sporns et al., 2005). At the macroscale, diffusion MRI tractography is the primary tool for mapping the human connectome (Van Essen et al., 2013). At the mesoscopic scale, the field has established viral tracing, considered the anatomical gold standard (Zingg et al., 2014), to provide the ground truth. This has been dramatically enhanced by technological innovations in high-resolution, whole-brain imaging (Ma et al., 2023; H. Wang et al., 2019; Zheng et al., 2024) and the creation of comprehensive connectivity atlases (Oh et al., 2014). The established approach, therefore, is to use this definitive meso-anatomical data to validate and constrain the large-scale pathways inferred from human tractography (Azadbakht et al., 2015; Schilling et al., 2019; Thomas et al., 2014). However, this structural validation is inherently limited, as diffusion MRI is blind to the direction and nature of information flow.

Our study operates within this validation paradigm but extends it into the functional domain. Building on foundational work that validated white matter BOLD signals (Ding et al., 2013, 2018; Y. Huang et al., 2023; Nozais et al., 2021), we use pRF modeling to move beyond signal detection and decode the informational content of callosal pathways. This allows us to reverse the conventional workflow: we employ viral tracing and light-sheet microscopy not to confirm a structural pathway, but to uncover the mesoanatomical mechanism, laminar segregation, for a functional principle first discovered in vivo with human fMRI. This cross-species approach is grounded in the deeply conserved developmental and molecular blueprint of the corpus callosum (Fenlon & Richards, 2015; Suárez et al., 2014, 2018), which exists despite divergence in scale and cognitive demand between mice and humans (Van Essen et al., 2019). While our findings establish segregation as a conserved principle, the human visual CC is likely more complex than the mouse's. Therefore, future investigations in non-human primates, which bridge this evolutionary gap, will be essential for a complete understanding of the visual callosal pathways.

Integrating White Matter with Laminar-Resolved Function

Bridging the gap between microscale circuit models and human cognition remains a central goal in neuroscience. By leveraging ultra-high-field imaging to resolve activity across cortical depths, laminar fMRI has emerged as a powerful tool in this endeavor. This technique allows for the in-vivo testing of canonical circuit models, for instance by dissociating feedforward, input-driven activity in middle cortical layers from feedback signals in superficial and deep layers (Liu et al., 2025; Yang et al., 2021; Yu et al., 2019). Our discovery of information segregation within white matter provides a critical new dimension to this framework. The combination of anatomically segregated white matter pathways with functionally specific cortical laminae presents a powerful synergy for human brain circuit researches. A question emerges, therefore, whether this segregation represents a general organizing principle that extends to other commissural and intrahemispheric tracts.

This capacity to resolve distinct information channels is of immediate relevance to clinical neuroscience. A significant innovation of our approach is its ability to delineate directional structural connectivity. For instance, following a unilateral stroke or traumatic brain injury, it becomes possible to assess not just if the CC is damaged, but precisely which directional pathways are compromised—those projecting from the lesioned hemisphere, those projecting to it, or both (Lim & Kang, 2015)(Parsons et al., 2023). This anatomical specificity is also poised to refine emerging functional measures like GM-WM connectivity analysis (Ji et al., 2025; P. Wang et al., 2022; Zu et al., 2024). By providing the structural blueprint of parallel conduits, our work enables the decomposition of a single tract's functional signal into pathway-specific components, a critical step for developing more sensitive biomarkers for conditions ranging from psychiatric disorders (Chu et al., 2025; Ji et al., 2023) to individual cognitive traits (J. Li et al., 2020). Although this study leveraged the high signal-to-noise ratio of 7T MRI, the rapid maturation of high-resolution fMRI sequences on 3T platforms promises to democratize this approach, accelerating its translation from basic science to widespread clinical application (Huber et al., 2023).

Developmental Origins of Segregated Callosal Architecture

The bundled architecture of the corpus callosum is established during development by a precise interplay of molecular and mechanical forces (Breau & Trembleau, 2023). For instance, cell adhesion molecules (CAMs) mediate the homophilic "zippering" of axons into cohesive fascicles (Moreland & Poulain, 2022). Simultaneously, the bundling is confined by repulsive cues, such as the interaction between Ephrin-A4 on callosal axons and EphA receptors in the surrounding tissue, which establishes a "permissive corridor" that prevents axonal migration and steers the entire tract across the midline (Gavrish et al., 2024; Yan et al., 2023). However, while these established mechanisms of fasciculation and guidance account for the formation of the callosal projection as a whole (Fenlon & Richards, 2015; Tezuka et al., 2022), they do not fully explain the highly organized internal structure we report. The subsequent refinement processes that establish the precise laminar segregation of ipsilateral and contralateral axons remain a key area for future investigation.

The Observation of Dual pRFs

The observation of dual pRFs is an expected consequence of signal pooling (Wandell & Winawer, 2015), where a single fMRI voxel averages signals from thousands of axons. In the FMA, this reflects

the known convergence of bilateral visual inputs near the vertical meridian, a phenomenon well-documented at the cortical boundaries (Caleo et al., 2013; Foubert, 2007; Schmidt et al., 2010). We therefore interpret these dual pRFs as the macroscale signature of localized zones where contralateral and ipsilateral fibers intermingle. Crucially, the sparse and localized nature of these integrative voxels, in contrast to the widespread distribution of single pRFs, reinforces our primary conclusion: the visual callosum operates predominantly as a set of parallel, segregated information conduits.

Topography for Midline and Perifoveal Vision

A key topographic principle revealed by our mapping is the preferential representation of the perifoveal visual field, coupled with a notable exclusion of the central 0.5° fovea (Supplementary Fig. S3C). This specific visuotopic arrangement appears to be a highly conserved feature of mammalian callosal organization. For instance, callosal neurons are densest in cortical regions representing the vertical meridian and near-foveal space in cats (Innocenti & Fiore, 1976; Milleret et al., 1994; Rochefort et al., 2009), macaques exhibit an expanded representation of the central visual field in callosal projection zones (Tanigawa et al., 2005), and callosal connections in rats align with eye-specific domains near the area centralis (Cusick & Lund, 1981; Laing et al., 2015). This cross-species consistency underscores the corpus callosum's fundamental role in fusing the two hemifields across the midline, where precise visuotopic alignment is essential for coherent perception.

4. Summary

Our study significantly advances the understanding of the FMA's functional topology in the context of interhemispheric visual integration. By revealing the presence of dual receptive fields and the unique parallel structure, we provide a new perspective on how visual information is processed across hemispheres. These findings not only enhance the existing literature on visual callosal connections but also open avenues for future research into the clinical implications of FMA connectivity in visual impairments. Further exploration of these connections could yield valuable insights into the neural mechanisms underlying visual perception and integration, with potential applications in understanding and treating visual disorders.

5. Methods

5.1. Subjects

The subjects included 178 young adults from the HCP (109 females, 69 males), aged 22 to 35. All participants completed 7T retinal topology fMRI and DTI data. All subjects had normal or corrected-to-normal visual acuity. Each subject was assigned a six-digit HCP ID.

5.2. HCP Datasets

Complete retinotopy datasets (six fMRI runs) were acquired for a total of 181 subjects (109 females, 72 males), aged 22–35, as part of the Young Adult HCP

(https://www.humanconnectome.org/study/hcp-young-adult/datareleases). To ensure data completeness and quality, we excluded 3 individuals with incomplete imaging records required in this study. The final cohort consisted of 178 participants (109 females, 69 males) with fully available 7 T retinotopic functional MRI (fMRI) and diffusion MRI (dMRI) data, which were used for subsequent analyses. The 7T retinotopy dataset includes four packages: (1) Retinotopy Task fMRI Functional Preprocessed Extended; (2) Structural Preprocessed for 7T, with the same spatial resolution and space as the fMRI data; (3) Diffusion Preprocessed, with 1.05 mm spatial resolution diffusion and structural data in native space. Stimuli for the retinotopy dataset comprised colorful object textures windowed through slowly moving apertures. Apertures and textures were generated at a resolution of 768 × 768 pixels and were constrained to a circular region with a diameter of 16.0. The apertures included clockwise or counterclockwise rotating wedges (RETCW, RETCCW), expanding or contracting rings (RETEXP, RETCON), and moving bars (RETBAR1, RETBAR2). For each stimulus type, a 5-minute fMRI scan was conducted, consisting of 300 volumes. The stimuli were presented in the following order: RETCCW, RETCW, RETEXP, RETCON, RETBAR1, and RETBAR2.

5.3. Preprocessing

We utilized the 7T retinotopy dataset from the Human Connectome Project (HCP), for which the data collection and standard preprocessing pipelines are extensively described elsewhere .(Benson et al., 2018; Glasser et al., 2013; T. Vu et al., 2017). The minimally preprocessed data provided for each subject included volumetric fMRI time series in MNI space (1.6-mm isotropic, TR=1s), high-resolution T1-weighted (T1w) structural images (0.7-mm isotropic), and diffusion-preprocessed data, including fractional anisotropy (FA) images.

To improve the accuracy of spatial normalization, particularly for T1w's limited contrast within the white matter, we implemented a custom registration procedure that leverages both T1w and FA images. This procedure began by individually intensity-normalizing the T1w and FA images for each subject to their respective global means. Subsequently, a composite structural image (T1w+FA) was generated for each subject by summing these two normalized volumes; this process was repeated for the MNI template's T1w and FA images to create a corresponding template composite. Nonlinear registration parameters were then computed by registering the individual's T1w+FA composite to the template's composite using the Advanced Normalization Tools (ANTs) package (Avants et al., 2008). In the final step, these derived transformation parameters were applied to the subject's original 1.6-mm fMRI data to bring them into the 1.0-mm MNI template space with high anatomical fidelity.

Prior to group averaging, several processing steps were applied to the time series of each individual subject. For each retinotopy run, the initial 8 volumes were discarded to ensure T1 signal stabilization. The remaining time series of each run was then normalized (e.g., to percent signal change) and linearly de-trended to correct for baseline shifts and signal drift. The cleaned runs for each subject were then concatenated in their original acquisition order. Finally, a single group-averaged fMRI dataset was created by averaging these fully preprocessed time series across all subjects for subsequent analyses.

5.4. Regions of Interest (ROIs)

A mask for the FMA was derived from the standard library provided by XTRACT, a component of the FMRIB Software Library (FSL). XTRACT offers a comprehensive set of predefined masks for white matter tractography, facilitating consistent and reproducible tract-based analysis(Jenkinson et al., 2012). The library and additional details can be accessed at https://fsl.fmrib.ox.ac.uk/fsl/fslwiki/XTRACT. The parietal CC connection mask was derived from Radwan et al.(Radwan et al., 2022). The whole-brain WM mask was generated using the automated segmentation tools provided by the FMRIB Software Library (FSL) (Smith et al., 2004). To avoid signal contamination from neighboring GM voxels, the FMA white matter mask was expanded inwards by 4 voxels. It is worth noting that the probabilistic maps were in MNI152 space. In this study, the T1 structural image in MNI152 space was registered with the asymmetric T1 image from the ICBM152 2009c template to generate a conversion file. Subsequently, the FMA fiber probabilistic tracking template from XTRACT was registered to the functional image space to extract the corresponding fMRI time series.

5.5. A Combined Model of pRF and Hemodynamic Response Functions (HRFs)

The Bayesian pRF framework allows the specification, estimation, and comparison of receptive field models, seeking the optimal balance between model accuracy and complexity. As Zeidman et al. described (Zeidman et al., 2018), neural activity at time t is modeled using a multivariate normal probability density function N. The response was summed over each illuminated pixel on the screen and scaled by a parameter. Structurally like the classical pRF approach, the Bayesian pRF framework comprises two components: a neuronal model describing the cortical response to visual stimulation, and a hemodynamic model accounting for neurovascular coupling and the resulting BOLD signal. The neural parameters and the elements of matrix are limited to a specific range of values through latent variables. These variables are utilized to compute the neuronal response. The specific parameter settings and model specification are comprehensively described below. the bayesian pRF model employs a series of spatial coordinates p_i to represent the set of stimulus positions U_t at time t.

$$U_t = \{p_1, \dots, p_n\}$$

$$p_i = (x \in R,\ y \in R)$$

The difference-of-Gaussians (DoG) model, which incorporates center excitation and surround suppression, is expressed as the difference between two Gaussian profiles. Here, the neural response z(t) is modeled as the sum of responses to all stimulus positions under the difference between two Gaussian profiles, each weighted by the multivariate normal probability density function $N(p_i|\mu,\Sigma)$: an excitatory center with gain β_c, center μ , and covariance Σ_c, and an inhibitory surround sharing the same center but with gain β_s and covariance Σ_s. Here, μ denotes the two-dimensional pRF center and Σ the covariance matrix determining receptive field size.

$$z(t) = \beta_c \sum_{p_i \in U_t} N(p_i \mid \mu, \Sigma_c) - \beta_s \sum_{p_i \in U_t} N(p_i \mid \mu, \Sigma_s)$$

$$N(p_i \mid \mu, \Sigma) = \frac{1}{\sqrt{(2\pi)^k |\Sigma|}} \exp\left(-\frac{1}{2}(p_i - \mu)^T \Sigma^{-1} (p_i - \mu)\right)$$

Latent variables l_p and l_θ were introduced to parameterize the pRF center in polar coordinates (ρ, θ). By applying the NCDF, the center position (μ_x, μ_y) was rigorously constrained to remain within the circular stimulus region across all optimization steps.

$$\rho = r \cdot \mathrm{NCDF}(l_\rho, 0,1)$$

$$\theta = 2\pi \cdot \mathrm{NCDF}(l_\theta, 0,1)$$

$$\mu_x = \rho \cdot \cos(\theta), \mu_y = \rho \cdot \sin(\theta), \mu = (\mu_x, \mu_y)$$

The size of the pRF was parameterized by its standard deviation σ, with the range constrained by the latent variable l_θ, and subsequently transformed within the model. Here, r and r_0 denote the radius of the circular stimulus region and the minimum allowable pRF size, respectively. The excitatory covariance matrix Σ_c and inhibitory surround Σ_s yields the DOG circular model.

$$\sigma = (r - r_0) \cdot \mathrm{NCDF}(l_\sigma, 0,1) + r_0$$

$$\Sigma_c = \begin{bmatrix} \sigma^2 & 0 \\ 0 & \sigma^2 \end{bmatrix}$$

$$\Sigma_s = \begin{bmatrix} (\sigma^2 + \sigma_d^2) & 0 \\ 0 & (\sigma^2 + \sigma_d^2) \end{bmatrix}$$

β_d and σ_d ensure positive center activation and negative surround response, enabling the model to capture both excitatory and suppressive components of receptive field organization.

$$\beta_s = \max(\beta_c - \beta_d, 0)$$

$$(\beta_c, \beta_d, \sigma_d) > 0$$

Zeidman et al. fed the predicted neural activity described above into the extended Ballon model to obtain the predicted BOLD response. In this study, the time series prediction was obtained by convolving $z(t)$ with a model of the hemodynamic response function (HRF; $h(t)$)(Boynton et al., 1996; Friston et al., 1998), which is composed of two gamma functions.

$$h(t) = \frac{t^{a_1 - 1} b_1^{a_1} e^{-b_1 t}}{\Gamma(a_1)} - \frac{t^{a_2 - 1} b_2^{a_2} e^{-b_2 t}}{d\Gamma(a_2)}$$

Γ in the above equation denotes the gamma function. The parameters a, b, c, d correspond to the shape and scale parameters of two probability density functions of the gamma distribution (see spm_Gpdf.m), one corresponding to the main response and the other to the undershoot. The parameter c determines the ratio of the response to the undershoot. As described by the spm_hrf function in SPM12, the parameters a, b, c, d are obtained by p with different meanings (see more in spm_hrf.m). Taking into account the variability of the hemodynamic function across regions and voxels, these parameters are given latent variables, analogous to the approach of Zeidman et al (Zeidman et al., 2018), thus adapting them to the optimization algorithm in the tool. These parameters also describe the properties of white matter HRFs.

5.6. Bayesian Model Comparison

In the Bayesian pRF computational framework, each voxel is given a set of model evidence, which is used as a metric for model evaluation. We compared the evidence from the HCP data under six different pRF models using a random effects analysis (RFX) model with the free energy described in Zeidman et al. (Stephan et al., 2009; Zeidman et al., 2018). Each model was given its Expected Probability and Protection Exceeding Probability (PXP). The former refers to the probability that random subject data will be produced by each model, while the latter represents the probability that each model will outperform all other models in a comparison.

5.7. FMA-Cortical Functional Connectivity and Gradients

Cortical ROI Definition and Connectivity Matrix Computation

To parcellate the visual cortex, we defined a set of 36 functional regions of interest (ROIs). These ROIs were created by intersecting a probabilistic atlas of the visual cortex (L. Wang et al., 2015) with retinotopic maps generated by Neuropythy (Benson & Winawer, 2018). The ROIs were organized on a grid spanning areas V1/V2 across four eccentricity bands ({0°, 2°, 8°, 20°}) and seven polar angle bins ({-30°, 30°, 90°, 150°, 210°, 270°, 330°}). Using the group-averaged retinotopy fMRI data, we extracted the mean time-series for each of the 36 cortical ROIs. A dense FMA-cortical functional connectivity matrix was then computed by calculating the Pearson correlation between each cortical ROI's time-series and the individual time-series of every voxel in the FMA. The resulting correlation values were subsequently stabilized using a Fisher's Z-transform.

Gradient Computation and Cortical Projection

The principal axes of functional connectivity variation within the FMA were identified by applying diffusion map embedding to the FMA-cortical connectivity matrix, through the BrainSpace Toolbox (Vos de Wael et al., 2020). This method produces a set of gradients, with the first gradient (G_1) representing the primary, most dominant axis of connectivity change across all FMA voxels.

To visualize how the FMA's primary functional gradient relates to the cortex, we projected it onto the cortical surface using a weighted summation approach adapted from prior work (Katsumi et al., 2023). The cortical projection map was calculated using the following formula:

$$P(c) = \sum_{v \in \mathrm{FMA}} \left(G_1(v) \times \mathrm{FC}(v, c) \right)$$

Where $P(c)$ is the projection value at a cortical vertex c, $G_1(v)$ is the score of an FMA voxel v on the principal gradient, and $FC(v, c)$ is the functional connectivity between them. Conceptually, this formula weights the cortical connectivity pattern of each FMA voxel by its score on the gradient. By summing these weighted maps, the resulting cortical projection $P(c)$ reveals the two opposing patterns of cortical connectivity that define the FMA's primary axis of functional organization.

5.8. Model Reliability Test

To evaluate the reliability of pRF estimates, we performed split-half analyses on group-averaged data across subjects and TR runs. The 178 subjects were randomly divided into two groups of equal size, and the data were averaged within each group. Within runs, the 300 TRs were split into the first and second 150 TRs, and then averaged across all subjects to create two independent group-averaged datasets. Voxels were thresholded under the single pRF model, and polar angle, pRF size, and HRF parameters were estimated independently for each half.

5.9. Fiber Tracking

All tractography was performed in DSI Studio (http://dsistudio.labsolver.org/) utilizing the group-averaged Human Connectome Project (HCP-1065) template (F.-C. Yeh et al., 2018). A deterministic fiber tracking algorithm based on quantitative anisotropy was employed to generate streamlines (F. C. Yeh et al., 2013). Tracking was seeded from all voxels within the FMA mask. To ensure comprehensive reconstruction of the fiber architecture, tracking was performed iteratively using a range of angular thresholds (30°, 40°, 50°, 60°, 70°, 80°, and 90°). Additional tracking parameters were held constant: a fractional anisotropy (FA) threshold of 0.15 was used to terminate pathways, the step size was set to 0.5 mm, and streamlines shorter than 20 mm or longer than 200 mm were discarded.

To delineate anatomical tracts corresponding to specific visual field representations, we employed a region-of-interest (ROI) and region-of-avoidance (ROA) strategy. The ROIs and ROAs were derived directly from our pRF functional maps, and the procedure was conducted separately for the left and right visual field pathways. For the left visual field pathway, a single seed volume (ROI) was created from all voxels functionally identified as representing the left visual field (located in both hemispheres), while an avoidance volume (ROA) was created from all voxels representing the right visual field. Streamlines were discarded if they entered the avoidance region. An analogous seeding and avoidance strategy was applied to delineate the right visual field pathway. For each pathway (left and right visual field), the streamlines generated across all angular thresholds were merged into a single comprehensive bundle. To remove anatomically implausible or spurious fibers, these final bundles were refined by removing any streamline clusters containing fewer than 100 streamlines.

5.10. Neuronal Viral Tracing

Animal and viruses

Male C57BL/6J mice aged 3-5 months obtained from SPF (Beijing) Biotechnology Co., Ltd were used for this study. The recombinant adeno-associated viruses (rAAV-hSyn-EGFP (AAV/9, 5.01E+12 vg /ml) and rAAV-hSyn-tdTomato (AAV/9, 3.75E+12 vg/ ml)) were purchased from BrainCase Co., Ltd. All animal experiments were approved by the Animal Care and Use Committee of the University of Science and Technology of China (USTCACUC21240122009).

Viral labeling

Viral injections were performed on anesthetized mice, which were subsequently mounted in an animal stereotaxic frame (RWD). A heating pad was utilized to maintain the animals' core body temperature at 36◦C. For anterograde tracing, specific viral constructs were bilaterally delivered into

the primary visual cortex (V1) of C57BL/6J male mice. The injection coordinates were established as: AP, −4.0 mm; ML, ±2.6 mm; and DV, −1.2 mm. Specifically, rAAV-hSyn-EGFP was infused into the right V1, and rAAV-hSyn-tdTomato into the left V1. Each injection consisted of 90 nL of virus, delivered via calibrated glass microelectrodes connected to an infusion pump at a constant rate of 10 nL/min. To minimize virus backflow along the injection track, the microsyringe was left in situ for 10 min following injection. Upon completion, the incision was sutured and the surgical site was sterilized with iodine.

Sample preparation and whole brain imaging

Three weeks post-viral injection, mice were anesthetized and transcardially perfused with 20 ml of 1×PBS (phosphate-buffered saline) twice, followed by 20 ml of 4% PFA (paraformaldehyde). Brains were then post-fixed in 4% PFA at 4 °C overnight and washed three times with 1×PBS. For hydrogel embedding, samples were immersed in a 1:1 solution of 4% HMS (Hydrogel Monomer Solution) and 20% BSA (bovine serum albumin). This solution was degassed in a vacuum pump for 10 min while centrifuge tubes were surrounded by ice. Samples were then polymerized in this solution at 37 °C for 4 hrs. All samples were subsequently sectioned into 300-μm-thick slices using a vibratome.

All slices underwent clearing in 4% SDS (Sodium Dodecyl Sulfate) with continuous shaking at 37 °C overnight. Following clearing, slices were washed three times with 0.3% PBST (1×PBS with 0.3% Triton X-100) and stored in 1×PBS at 4 °C. The processed slices were then sequentially mounted onto hydrophilic-treated glass panes. After applying vacuum-degassed 4% HMS solution in a fume hood, slices were covered with hydrophobic-treated glass slides. These samples were transferred to a 37 °C incubator and polymerized for 4 hrs. Subsequently, the samples were immersed in a high-refractive-index matching solution. The cleared slices were then imaged using VISoR (Volumetric Imaging with Synchronized on-the-fly-scan and Readout). Imaging was performed sequentially using 488 nm and 561 nm excitation for virus-labeled signal acquisition, and 405 nm excitation to capture tissue autofluorescence. Image stacks were acquired at an isotropic voxel size of $1\times1\times3.5\ \mu m^3$.

Whole brain reconstruction

The brain reconstruction pipeline comprised five sequential stages (Ma et al., 2023; Zheng et al., 2024): (1) Image columns are generated by the actual stacking of coordinates. Whole-brain slices were computationally reassembled from sequentially acquired image columns by applying pre-calibrated distortion correction coefficients and spatially registering overlapping fiducial markers to ground-truth coordinates. (2) The upper and lower image planes of each contrast-enhanced slice were algorithmically reconstructed through linear regression and interpolation. (3) Adjacent slices were co-registered using a hybrid approach that combines rigid transformation with B-spline-based non-rigid deformation to align fine-scale textural features and edge contours. (4) Displacement vector fields between neighboring slices were iteratively optimized to mitigate error propagation across the volumetric dataset. (5) A moving-least-squares algorithm was applied to minimize residual slice-level distortions while preserving intrinsic tissue morphology.

Quantification of spatial colocalization

To assess the degree of spatial colocalization between the two fluorescently labeled fiber populations, we calculated the Dice coefficient (D) and the Jaccard index (J) based on based on volumetric overlap of red and green channel-labeled projection. The metrics are defined as:

$$D = 2 \times \frac{(A \cap B)}{(A \cup B)}$$

$$J = \frac{(A \cap B)}{(A \cup B)}$$

Where A and B denote the 3D volumes of green and red fiber tracts respectively, $(A \cap B)$ represents their volumetric overlap, and $(A \cup B)$represents the combined volumetric space occupied by both tracts. The Jaccard index (J) and Dice coefficient (D) were calculated from binarized volumetric masks, with both metrics yielding values from 0 (complete spatial segregation) to 1 (perfect volumetric colocalization).

6. Data availability

The data and code with be shared upon requests.

7. Acknowledgements

This work was partially supported by National Science and Technology Innovation 2030 Major Program 2022ZD0204801, the Institute of Artificial Intelligence of Hefei Comprehensive National Science Center (23YGXT004, Y1022502).

8. References

Avants, B. B., Epstein, C. L., Grossman, M., & Gee, J. C. (2008). Symmetric diffeomorphic image registration with cross-correlation: Evaluating automated labeling of elderly and neurodegenerative brain. *Medical Image Analysis*, *12*(1), 26–41. https://doi.org/10.1016/j.media.2007.06.004

Azadbakht, H., Parkes, L. M., Haroon, H. A., Augath, M., Logothetis, N. K., de Crespigny, A., D'Arceuil, H. E., & Parker, G. J. M. (2015). Validation of High-Resolution Tractography Against In Vivo Tracing in the Macaque Visual Cortex. *Cerebral Cortex*, *25*(11), 4299–4309. https://doi.org/10.1093/cercor/bhu326

Benson, N. C., Jamison, K. W., Arcaro, M. J., Vu, A. T., Glasser, M. F., Coalson, T. S., Van Essen, D. C., Yacoub, E., Ugurbil, K., Winawer, J., & Kay, K. (2018). The Human Connectome Project 7 Tesla retinotopy dataset: Description and population receptive field analysis. *Journal of Vision*, *18*(13), 23. https://doi.org/10.1167/18.13.23

Benson, N. C., & Winawer, J. (2018). Bayesian analysis of retinotopic maps. *eLife*, *7*. https://doi.org/10.7554/eLife.40224

Bocci, T., Pietrasanta, M., Cerri, C., Restani, L., Caleo, M., & Sartucci, F. (2014). Visual callosal connections: Role in visual processing in health and disease. *Reviews in the Neurosciences*, *25*(1), 113–127. https://doi.org/10.1515/revneuro-2013-0025

Boynton, G. M., Engel, S. A., Glover, G. H., & Heeger, D. J. (1996). Linear systems analysis of functional magnetic resonance imaging in human V1. *The Journal of Neuroscience: The Official Journal of the Society for Neuroscience*, *16*(13), 4207–4221. https://doi.org/10.1523/JNEUROSCI.16-13-04207.1996

Breau, M. A., & Trembleau, A. (2023). Chemical and mechanical control of axon fasciculation and defasciculation. *Seminars in Cell & Developmental Biology*, *140*, 72–81. https://doi.org/10.1016/j.semcdb.2022.06.014

Caleo, M., Innocenti, G. M., & Ptito, M. (2013). Physiology and Plasticity of Interhemispheric Connections. *Neural Plasticity*, *2013*, 176183. https://doi.org/10.1155/2013/176183

Chu, T., Si, X., Song, X., Che, K., Dong, F., Guo, Y., Chen, D., Yao, W., Zhao, F., Xie, H., Shi, Y., Ma, H., Ming, D., & Mao, N. (2025). Understanding structural-functional connectivity coupling in patients with major depressive disorder: A white matter perspective. *Journal of Affective Disorders*, *373*, 219–226. https://doi.org/10.1016/j.jad.2024.12.082

Chung, S., Fieremans, E., Novikov, D. S., & Lui, Y. W. (2024). Microstructurally informed subject-specific parcellation of the corpus callosum using axonal water fraction. *Brain Structure and Function*, *230*(1), 1. https://doi.org/10.1007/s00429-024-02872-7

Cusick, C. G., & Lund, R. D. (1981). The distribution of the callosal projection to the occipital visual cortex in rats and mice. *Brain Research*, *214*(2), 239–259. https://doi.org/10.1016/0006-8993(81)91192-6

Ding, Z., Huang, Y., Bailey, S. K., Gao, Y., Cutting, L. E., Rogers, B. P., Newton, A. T., & Gore, J. C. (2018). Detection of synchronous brain activity in white matter tracts at rest and under functional loading. *Proceedings of the National Academy of Sciences*, *115*(3), 595–600. https://doi.org/10.1073/pnas.1711567115

Ding, Z., Newton, A. T., Xu, R., Anderson, A. W., Morgan, V. L., & Gore, J. C. (2013). Spatio-Temporal Correlation Tensors Reveal Functional Structure in Human Brain. *PLOS One*, *8*(12), e82107. https://doi.org/10.1371/journal.pone.0082107

Fenlon, L. R., & Richards, L. J. (2015). Contralateral targeting of the corpus callosum in normal and pathological brain function. *Trends in Neurosciences*, *38*(5), 264–272. https://doi.org/10.1016/j.tins.2015.02.007

Foubert, L. (2007). *Spatio-temporal characteristics of the visual interhemispheric integration via the corpus callosum: Computational modeling & optical imaging approaches* [Phdthesis, Université Pierre et Marie Curie - Paris VI]. https://theses.hal.science/tel-00811495

Fraser, L. M., Stevens, M. T., Beyea, S. D., & D'Arcy, R. C. N. (2012). White versus gray matter: fMRI hemodynamic responses show similar characteristics, but differ in peak amplitude. *BMC Neuroscience*, *13*(1), 91. https://doi.org/10.1186/1471-2202-13-91

Friston, K. J., Fletcher, P., Josephs, O., Holmes, A., Rugg, M. D., & Turner, R. (1998). Event-related fMRI: Characterizing differential responses. *NeuroImage*, *7*(1), 30–40. https://doi.org/10.1006/nimg.1997.0306

Gavrish, M., Kustova, A., Celis Suescún, J. C., Bessa, P., Mitina, N., & Tarabykin, V. (2024). Molecular mechanisms of corpus callosum development: A four-step journey. *Frontiers in Neuroanatomy*, *17*. https://www.frontiersin.org/articles/10.3389/fnana.2023.1276325

Gazzaniga, M. S. (2000). Cerebral specialization and interhemispheric communication: Does the corpus callosum enable the human condition? *Brain*, *123*(7), 1293–1326. https://doi.org/10.1093/brain/123.7.1293

Glasser, M. F., Sotiropoulos, S. N., Wilson, J. A., Coalson, T. S., Fischl, B., Andersson, J. L., Xu, J., Jbabdi, S., Webster, M., Polimeni, J. R., Van Essen, D. C., Jenkinson, M., & WU-Minn HCP Consortium. (2013). The minimal preprocessing pipelines for the Human Connectome Project. *NeuroImage*, *80*, 105–124. https://doi.org/10.1016/j.neuroimage.2013.04.127

Goldstein, A., Covington, B. P., Mahabadi, N., & Mesfin, F. B. (2025). Neuroanatomy, Corpus Callosum. In *StatPearls*. StatPearls Publishing. http://www.ncbi.nlm.nih.gov/books/NBK448209/

Huang, H., Jiang, Y., Li, H., Wu, H., Feng, X., Gong, J., Jiang, S., Yao, D., & Luo, C. (2024). Functional organization of the human corpus callosum unveiled with BOLD-fMRI gradients. *Imaging Neuroscience*, *2*, 1–22. https://doi.org/10.1162/imag_a_00115

Huang, Y., Wei, P.-H., Xu, L., Chen, D., Yang, Y., Song, W., Yi, Y., Jia, X., Wu, G., Fan, Q., Cui, Z., & Zhao, G. (2023). Intracranial electrophysiological and structural basis of BOLD functional connectivity in human brain white matter. *Nature Communications*, *14*(1), 3414. https://doi.org/10.1038/s41467-023-39067-3

Huber, L. (Renzo), Kronbichler, L., Stirnberg, R., Ehses, P., Stöcker, T., Fernández-Cabello, S., Poser, B. A., & Kronbichler, M. (2023). Evaluating the capabilities and challenges of layer-fMRI VASO at 3T. *Aperture Neuro*, *3*, 10.52294/001c.85117. https://doi.org/10.52294/001c.85117

Innocenti, G. M., & Fiore, L. (1976). Morphological correlates of visual field transformation in the corpus callosum. *Neuroscience Letters*, *2*(5), 245–252. https://doi.org/10.1016/0304-3940(76)90155-5

Jenkinson, M., Beckmann, C. F., Behrens, T. E. J., Woolrich, M. W., & Smith, S. M. (2012). FSL. *NeuroImage*, *62*(2), 782–790. https://doi.org/10.1016/j.neuroimage.2011.09.015

Ji, G.-J., Cui, Z., D'Arcy, R. C. N., Liao, W., Biswal, B. B., Zhang, Q., Luo, C., Zang, Y.-F., Ding, Z., Zuo, X.-N., Gore, J. C., & Wang, K. (2025). Imaging brain white matter function using resting-state functional MRI. *Science Bulletin*, *70*(9), 1384–1388. https://doi.org/10.1016/j.scib.2024.11.001

Ji, G.-J., Sun, J., Hua, Q., Zhang, L., Zhang, T., Bai, T., Wei, L., Wang, X., Qiu, B., Wang, A., Sun, H., Liao, W., Yu, F., Zhu, C., Tian, Y., He, K., & Wang, K. (2023). White matter dysfunction in psychiatric disorders is associated with neurotransmitter and genetic profiles. *Nature Mental Health*, *1*(9), Article 9. https://doi.org/10.1038/s44220-023-00111-2

Katsumi, Y., Zhang, J., Chen, D., Kamona, N., Bunce, J. G., Hutchinson, J. B., Yarossi, M., Tunik, E., Dickerson, B. C., Quigley, K. S., & Barrett, L. F. (2023). Correspondence of functional connectivity gradients across human isocortex, cerebellum, and hippocampus. *Communications Biology*, *6*(1), 401. https://doi.org/10.1038/s42003-023-04796-0

Laing, R. J., Turecek, J., Takahata, T., & Olavarria, J. F. (2015). Identification of Eye-Specific Domains and Their Relation to Callosal Connections in Primary Visual Cortex of Long Evans Rats. *Cerebral Cortex*, *25*(10), 3314–3329. https://doi.org/10.1093/cercor/bhu128

Li, J., Biswal, B. B., Meng, Y., Yang, S., Duan, X., Cui, Q., Chen, H., & Liao, W. (2020). A neuromarker of individual general fluid intelligence from the white-matter functional connectome. *Translational Psychiatry*, *10*(1), 147. https://doi.org/10.1038/s41398-020-0829-3

Li, M., Newton, A. T., Anderson, A. W., Ding, Z., & Gore, J. C. (2019). Characterization of the hemodynamic response function in white matter tracts for event-related fMRI. *Nature Communications*, *10*(1), 1140. https://doi.org/10.1038/s41467-019-09076-2

Lim, J.-S., & Kang, D.-W. (2015). Stroke Connectome and Its Implications for Cognitive and Behavioral Sequela of Stroke. *Journal of Stroke*, *17*(3), 256–267. https://doi.org/10.5853/jos.2015.17.3.256

Liu, P., Doehler, J., Henschke, J. U., Northall, A., Knaf-Serian, A., Loaiza-Carvajal, L. C., Budinger, E., Schwarzkopf, D. S., Speck, O., Pakan, J. M. P., & Kuehn, E. (2025). Layer-specific changes in sensory cortex across the lifespan in mice and humans. *Nature Neuroscience*, *28*(9), 1978–1989. https://doi.org/10.1038/s41593-025-02013-1

Ma, C., Xia, D., Huang, S., Du, Q., Liu, J., Zhang, B., Zhu, Q., Bi, G., Wang, H., & Xu, R. X. (2023). High precision vibration sectioning for 3D imaging of the whole central nervous system. *Journal of Neuroscience Methods*, *399*, 109966. https://doi.org/10.1016/j.jneumeth.2023.109966

Milleret, C., Houzel, J. C., & Buser, P. (1994). Pattern of Development of the Callosal Transfer of Visual Information to Cortical Areas 17 and 18 in the Cat. *European Journal of Neuroscience*, *6*(2), 193–202. https://doi.org/10.1111/j.1460-9568.1994.tb00261.x

Moreland, T., & Poulain, F. E. (2022). To Stick or Not to Stick: The Multiple Roles of Cell Adhesion Molecules in Neural Circuit Assembly. *Frontiers in Neuroscience*, *16*. https://doi.org/10.3389/fnins.2022.889155

Nozais, V., Forkel, S. J., Foulon, C., Petit, L., & Thiebaut de Schotten, M. (2021). Functionnectome as a framework to analyse the contribution of brain circuits to fMRI. *Communications Biology*, *4*(1), 1035. https://doi.org/10.1038/s42003-021-02530-2

Oh, S. W., Harris, J. A., Ng, L., Winslow, B., Cain, N., Mihalas, S., Wang, Q., Lau, C., Kuan, L., Henry, A. M., Mortrud, M. T., Ouellette, B., Nguyen, T. N., Sorensen, S. A., Slaughterbeck, C. R., Wakeman, W., Li, Y., Feng, D., Ho, A., … Zeng, H. (2014). A mesoscale connectome of the mouse brain. *Nature*, *508*(7495), 207–214. https://doi.org/10.1038/nature13186

Parsons, N., Irimia, A., Amgalan, A., Ugon, J., Morgan, K., Shelyag, S., Hocking, A., Poudel, G., & Caeyenberghs, K. (2023). Structural-functional connectivity bandwidth predicts processing speed in mild traumatic brain Injury: A multiplex network analysis. *NeuroImage: Clinical*, *38*, 103428. https://doi.org/10.1016/j.nicl.2023.103428

Radwan, A. M., Sunaert, S., Schilling, K., Descoteaux, M., Landman, B. A., Vandenbulcke, M., Theys, T., Dupont, P., & Emsell, L. (2022). An atlas of white matter anatomy, its variability, and reproducibility based on constrained spherical deconvolution of diffusion MRI. *NeuroImage*, *254*, 119029. https://doi.org/10.1016/j.neuroimage.2022.119029

Rivest, J., Cavanagh, P., & Lassonde, M. (1994). Interhemispheric depth judgement. *Neuropsychologia*, *32*(1), 69–76. https://doi.org/10.1016/0028-3932(94)90069-8

Rochefort, N. L., Buzás, P., Quenech'du, N., Koza, A., Eysel, U. T., Milleret, C., & Kisvárday, Z. F. (2009). Functional Selectivity of Interhemispheric Connections in Cat Visual Cortex. *Cerebral Cortex*, *19*(10), 2451–2465. https://doi.org/10.1093/cercor/bhp001

Santana, C., Abreu, T., Rodrigues, J., Julio, P., Appenzeller, S., & Rittner, L. (2023). DTI-based Corpus Callosum parcellation using the Tensorial Morphological Gradient and Self-Organizing Maps. *2023 19th International Symposium on Medical Information Processing and Analysis (SIPAIM)*, 1–5. https://doi.org/10.1109/SIPAIM56729.2023.10373443

Schilling, K. G., Daducci, A., Maier-Hein, K., Poupon, C., Houde, J. C., Nath, V., Anderson, A. W., Landman, B. A., & Descoteaux, M. (2019). Challenges in diffusion MRI tractography—Lessons learned from international benchmark competitions. *Magn Reson Imaging*, *57*, 194–209. https://doi.org/10.1016/j.mri.2018.11.014

Schmidt, K. E., Lomber, S. G., & Innocenti, G. M. (2010). Specificity of Neuronal Responses in Primary Visual Cortex Is Modulated by Interhemispheric CorticoCortical Input. *Cerebral Cortex (New York, NY)*, *20*(12), 2776–2786. https://doi.org/10.1093/cercor/bhq024

Schulte, T., & Müller-Oehring, E. M. (2010). Contribution of Callosal Connections to the Interhemispheric Integration of Visuomotor and Cognitive Processes. *Neuropsychology Review*, *20*(2), 174–190. https://doi.org/10.1007/s11065-010-9130-1

Sincich, L. C., & Blasdel, G. G. (2001). Oriented Axon Projections in Primary Visual Cortex of the Monkey. *The Journal of Neuroscience*, *21*(12), 4416–4426. https://doi.org/10.1523/JNEUROSCI.21-12-04416.2001

Smith, S. M., Jenkinson, M., Woolrich, M. W., Beckmann, C. F., Behrens, T. E. J., Johansen-Berg, H., Bannister, P. R., De Luca, M., Drobnjak, I., Flitney, D. E., Niazy, R. K., Saunders, J., Vickers, J., Zhang, Y., De Stefano, N., Brady, J. M., & Matthews, P. M. (2004). Advances in functional and structural MR image analysis and implementation as FSL. *NeuroImage*, *23*, S208–S219. https://doi.org/10.1016/j.neuroimage.2004.07.051

Sporns, O., Tononi, G., & Kötter, R. (2005). The Human Connectome: A Structural Description of the Human Brain. *PLoS Computational Biology*, *1*(4), e42. https://doi.org/10.1371/journal.pcbi.0010042

Stephan, K. E., Penny, W. D., Daunizeau, J., Moran, R. J., & Friston, K. J. (2009). Bayesian model selection for group studies. *Neuroimage*, *46*(4), 1004–1017. https://doi.org/10.1016/j.neuroimage.2009.03.025

Suárez, R., Gobius, I., & Richards, L. J. (2014). Evolution and development of interhemispheric connections in the vertebrate forebrain. *Frontiers in Human Neuroscience*, *8*. https://doi.org/10.3389/fnhum.2014.00497

Suárez, R., Paolino, A., Fenlon, L. R., Morcom, L. R., Kozulin, P., Kurniawan, N. D., & Richards, L. J. (2018). A pan-mammalian map of interhemispheric brain connections predates the evolution of the corpus callosum. *Proceedings of the National Academy of Sciences*, *115*(38), 9622–9627. https://doi.org/10.1073/pnas.1808262115

T. Vu, A., Jamison, K., Glasser, M. F., Smith, S. M., Coalson, T., Moeller, S., Auerbach, E. J., Uğurbil, K., & Yacoub, E. (2017). Tradeoffs in pushing the spatial resolution of fMRI for the 7T Human Connectome Project. *NeuroImage*, *154*, 23–32. https://doi.org/10.1016/j.neuroimage.2016.11.049

Tanigawa, H., Wang, Q., & Fujita, I. (2005). Organization of Horizontal Axons in the Inferior Temporal Cortex and Primary Visual Cortex of the Macaque Monkey. *Cerebral Cortex*, *15*(12), 1887–1899. https://doi.org/10.1093/cercor/bhi067

Tezuka, Y., Hagihara, K. M., Ohki, K., Hirano, T., & Tagawa, Y. (2022). Developmental stage-specific spontaneous activity contributes to callosal axon projections. *eLife*, *11*, e72435. https://doi.org/10.7554/eLife.72435

Thomas, C., Ye, F. Q., Irfanoglu, M. O., Modi, P., Saleem, K. S., Leopold, D. A., & Pierpaoli, C. (2014). Anatomical accuracy of brain connections derived from diffusion MRI tractography is inherently limited. *Proceedings of the National Academy of Sciences*, *111*(46), 16574–16579. https://doi.org/10.1073/pnas.1405672111

Van Essen, D. C., Donahue, C. J., Coalson, T. S., Kennedy, H., Hayashi, T., & Glasser, M. F. (2019). Cerebral cortical folding, parcellation, and connectivity in humans, nonhuman primates, and mice. *Proceedings of the National Academy of Sciences*, *116*(52), 26173–26180. https://doi.org/10.1073/pnas.1902299116

Van Essen, D. C., Smith, S. M., Barch, D. M., Behrens, T. E., Yacoub, E., Ugurbil, K., & W. U-Minn HCP Consortium. (2013). The WU-Minn Human Connectome Project: An overview. *Neuroimage*, *80*, 62–79. https://doi.org/10.1016/j.neuroimage.2013.05.041

Vos de Wael, R., Benkarim, O., Paquola, C., Lariviere, S., Royer, J., Tavakol, S., Xu, T., Hong, S.-J., Langs, G., Valk, S., Misic, B., Milham, M., Margulies, D., Smallwood, J., & Bernhardt, B. C. (2020). BrainSpace: A toolbox for the analysis of macroscale gradients in neuroimaging and connectomics datasets. *Communications Biology*, *3*(1), 1–10. https://doi.org/10.1038/s42003-020-0794-7

Wandell, B. A., Dumoulin, S. O., & Brewer, A. A. (2007). Visual field maps in human cortex. *Neuron*, *56*(2), 366–383. https://doi.org/10.1016/j.neuron.2007.10.012

Wandell, B. A., & Winawer, J. (2015). Computational neuroimaging and population receptive fields. *Trends in Cognitive Sciences*, *19*(6), 349–357. https://doi.org/10.1016/j.tics.2015.03.009

Wang, H., Wang, X., Wang, Y., Zhang, D., Yang, Y., Zhou, Y., Qiu, B., & Zhang, P. (2023). White matter BOLD signals at 7 Tesla reveal visual field maps in optic radiation and vertical occipital fasciculus. *NeuroImage*, *269*, 119916. https://doi.org/10.1016/j.neuroimage.2023.119916

Wang, H., Zhu, Q., Ding, L., Shen, Y., Yang, C.-Y., Xu, F., Shu, C., Guo, Y., Xiong, Z., Shan, Q., Jia, F., Su, P., Yang, Q.-R., Li, B., Cheng, Y., He, X., Chen, X., Wu, F., Zhou, J.-N., … Bi, G.-Q. (2019). Scalable volumetric imaging for ultrahigh-speed brain mapping at synaptic resolution. *National Science Review*, *6*(5), 982–992. https://doi.org/10.1093/nsr/nwz053

Wang, L., Mruczek, R. E., Arcaro, M. J., & Kastner, S. (2015). Probabilistic Maps of Visual Topography in Human Cortex. *Cerebral Cortex*, *25*(10), 3911–3931. https://doi.org/10.1093/cercor/bhu277

Wang, P., Wang, J., Michael, A., Wang, Z., Klugah-Brown, B., Meng, C., & Biswal, B. B. (2022). White Matter Functional Connectivity in Resting-State fMRI: Robustness, Reliability, and Relationships to Gray Matter. *Cerebral Cortex*, *32*(8), 1547–1559. https://doi.org/10.1093/cercor/bhab181

Wang, Y., Wang, H., Hu, S., Nguchu, B. A., Zhang, D., Chen, S., Ji, Y., Qiu, B., & Wang, X. (2024). Sub-bundle based analysis reveals the role of human optic radiation in visual working memory. *Human Brain Mapping*, *45*(11), e26800. https://doi.org/10.1002/hbm.26800

Yan, K., Bormuth, I., Bormuth, O., Tutukova, S., Renner, A., Bessa, P., Schaub, T., Rosário, M., & Tarabykin, V. (2023). TrkB-dependent EphrinA reverse signaling regulates callosal axon fasciculate growth downstream of Neurod2/6. *Cerebral Cortex*, *33*(5), 1752–1767. https://doi.org/10.1093/cercor/bhac170

Yang, J., Huber, L., Yu, Y., & Bandettini, P. A. (2021). Linking cortical circuit models to human cognition with laminar fMRI. *Neuroscience & Biobehavioral Reviews*, *128*, 467–478. https://doi.org/10.1016/j.neubiorev.2021.07.005

Yeh, F. C., Verstynen, T. D., Wang, Y., Fernandez-Miranda, J. C., & Tseng, W. Y. (2013). Deterministic diffusion fiber tracking improved by quantitative anisotropy. *PLoS One*, *8*(11), e80713. https://doi.org/10.1371/journal.pone.0080713

Yeh, F.-C., Panesar, S., Fernandes, D., Meola, A., Yoshino, M., Fernandez-Miranda, J. C., Vettel, J. M., & Verstynen, T. (2018). Population-averaged atlas of the macroscale human structural connectome and its network topology. *NeuroImage*, *178*, 57–68. https://doi.org/10.1016/j.neuroimage.2018.05.027

Yu, Y., Huber, L., Yang, J., Jangraw, D. C., Handwerker, D. A., Molfese, P. J., Chen, G., Ejima, Y., Wu, J., & Bandettini, P. A. (2019). Layer-specific activation of sensory input and predictive feedback in the human primary somatosensory cortex. *Science Advances*, *5*(5), eaav9053. https://doi.org/10.1126/sciadv.aav9053

Zeidman, P., Silson, E. H., Schwarzkopf, D. S., Baker, C. I., & Penny, W. (2018). Bayesian population receptive field modelling. *Neuroimage*, *180*, 173–187. https://doi.org/10.1016/j.neuroimage.2017.09.008

Zhao, Y., Yang, Z., Ding, Z., & Su, J. (2023). A Riemannian Framework for Structurally Curated Functional Clustering of Brain White Matter Fibers. *IEEE Transactions on Medical Imaging*, *42*(8), 2414–2424. IEEE Transactions on Medical Imaging. https://doi.org/10.1109/TMI.2023.3252269

Zheng, W., Mu, H., Chen, Z., Liu, J., Xia, D., Cheng, Y., Jing, Q., Lau, P.-M., Tang, J., Bi, G.-Q., Wu, F., & Wang, H. (2024). NEATmap: A high-efficiency deep learning approach for whole mouse brain neuronal activity trace mapping. *National Science Review*, *11*(5), nwae109. https://doi.org/10.1093/nsr/nwae109

Zingg, B., Hintiryan, H., Gou, L., Song, M. Y., Bay, M., Bienkowski, M. S., Foster, N. N., Yamashita, S., Bowman, I., Toga, A. W., & Dong, H.-W. (2014). Neural networks of the mouse neocortex. *Cell*, *156*(5), 1096–1111. https://doi.org/10.1016/j.cell.2014.02.023

Zu, Z., Choi, S., Zhao, Y., Gao, Y., Li, M., Schilling, K. G., Ding, Z., & Gore, J. C. (2024). The missing third dimension—Functional correlations of BOLD signals incorporating white matter. *Science Advances*, *10*(4), eadi0616. https://doi.org/10.1126/sciadv.adi0616

9. Supplementary

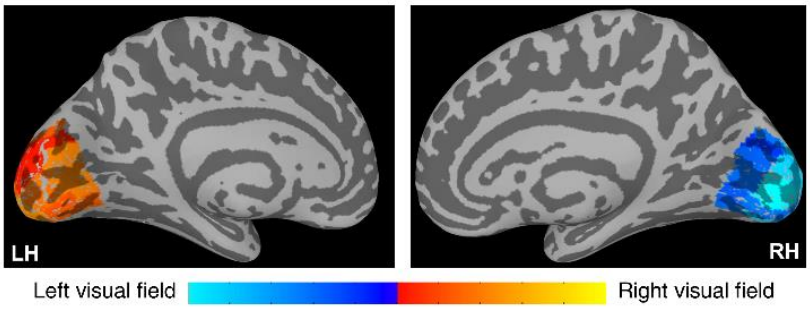

Fig S1. Gradients functional connectivity of forceps major (FMA) projection in the visual cortex. The visual cortex of the left hemisphere processes the right visual field information, while the visual cortex of the right hemisphere processes the left visual field information.

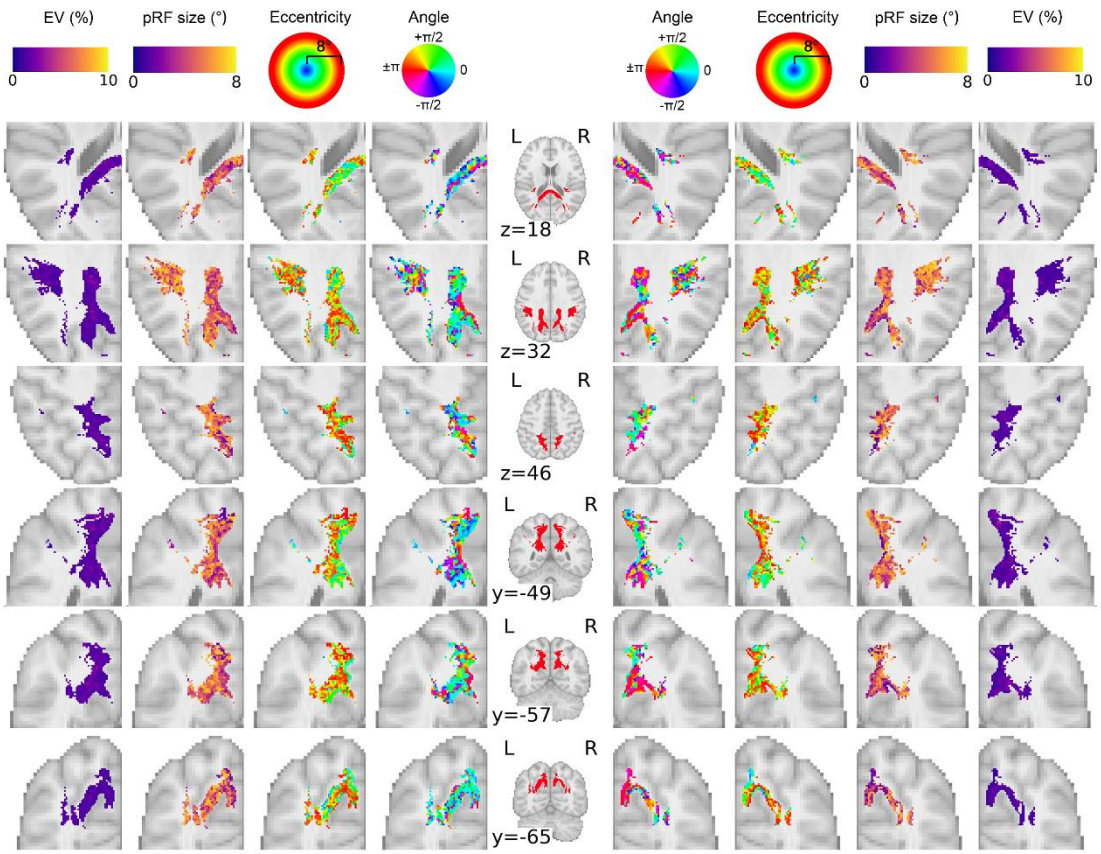

Fig S2. Population receptive field (pRF) parameter maps in the parietal corpus callosum (CC) connection fiber bundle. Visual field maps and explained variance maps are shown in selected axial and coronal views, with all voxels within the region of interest (ROI) displayed. Columns, from the center to the outer sides, display: (i) the parietal CC connection fiber bundle mask, (ii) polar angle maps (in degrees of visual angle), (iii) eccentricity maps (in degrees of visual angle), (iv) pRF size (σ, in degrees of visual angle), and (v) explained variance (%). Rows 2–4 (from top to bottom) correspond to axial slices from dorsal to ventral; rows 5–7 (from top to bottom) correspond to coronal slices from anterior to posterior. All maps are overlaid on the ICBM 152 2009c standard brain template, with Montreal Neurological Institute (MNI) coordinates for the z-axis (axial views) and y-axis (coronal views) shown in millimeters.

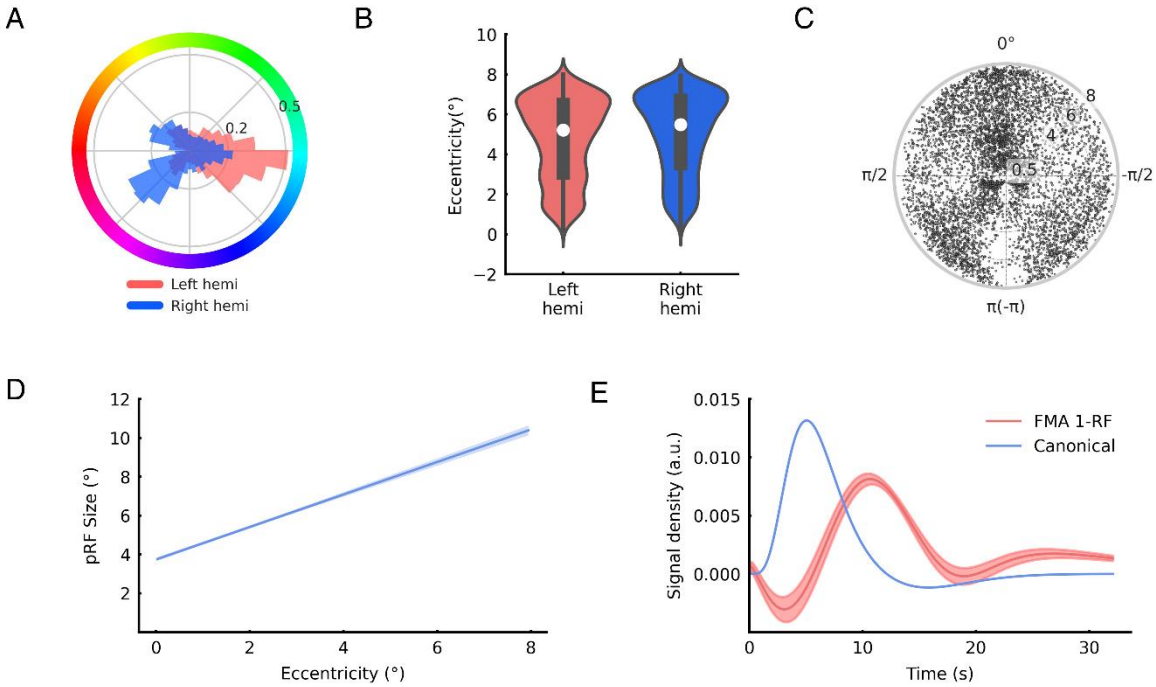

Fig S3. Visual field map properties, hemodynamic response functions (HRFs), and gradient-based validation of angular characteristics in the forceps major (FMA) fiber bundle. (A) Polar angle distribution maps for the FMA, with voxels from the right hemisphere shown in pink and those from the left hemisphere in blue. (B) Violin plots showing the distribution of pRF eccentricity (in degrees of visual angle) within the FMA, white dots indicate the median values. (C) Distribution of pRF eccentricity across polar angle bins, illustrating the spatial relationship between angular position and eccentricity. (D) Relationship between pRF size (σ, in degrees of visual angle) and eccentricity. Solid lines indicate fitted linear regression models, and shaded areas denote bootstrapped 95% confidence intervals. (E) Fitted hemodynamic response function (HRF) curves for the FMA. Solid lines represent the mean HRF across voxels, and shaded areas represent bootstrapped 95% confidence intervals.

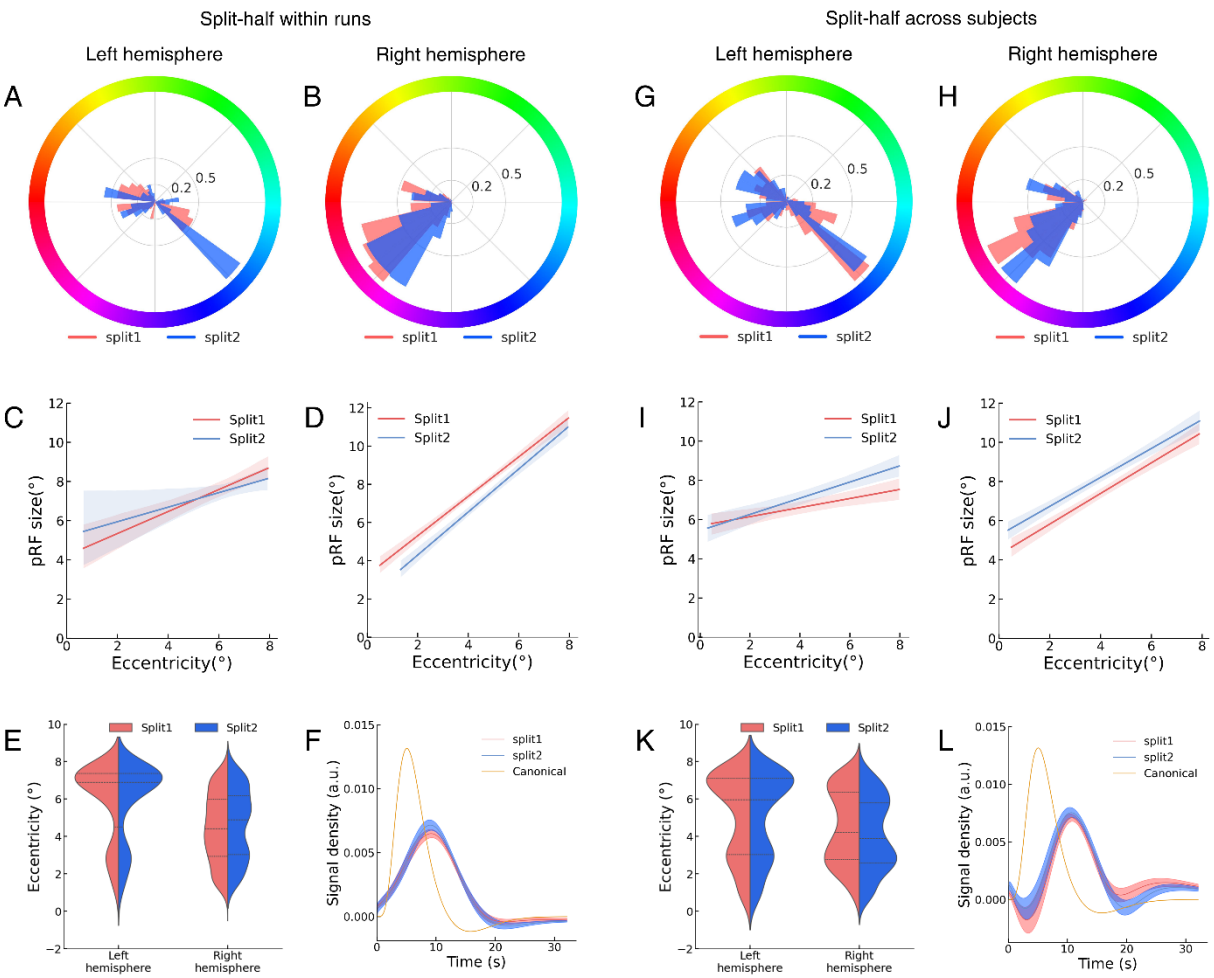

Fig. S4. Results of split-half analyses across subjects and within runs using group-averaged data. (A&B) Comparison of the polar angle distribution of FMA estimated from the data of two halves of runs. Split 1 and 2 are represented in pink and blue, respectively. (C&D) The correlation between pRF size and eccentricity in the left and right hemispheres. (E) Eccentricity distribution and (F) HRFs in FMA for the split-runs analysis. (G-L) Split-subject results for FMA. Shaded areas represent bootstrapped 95% confidence intervals.

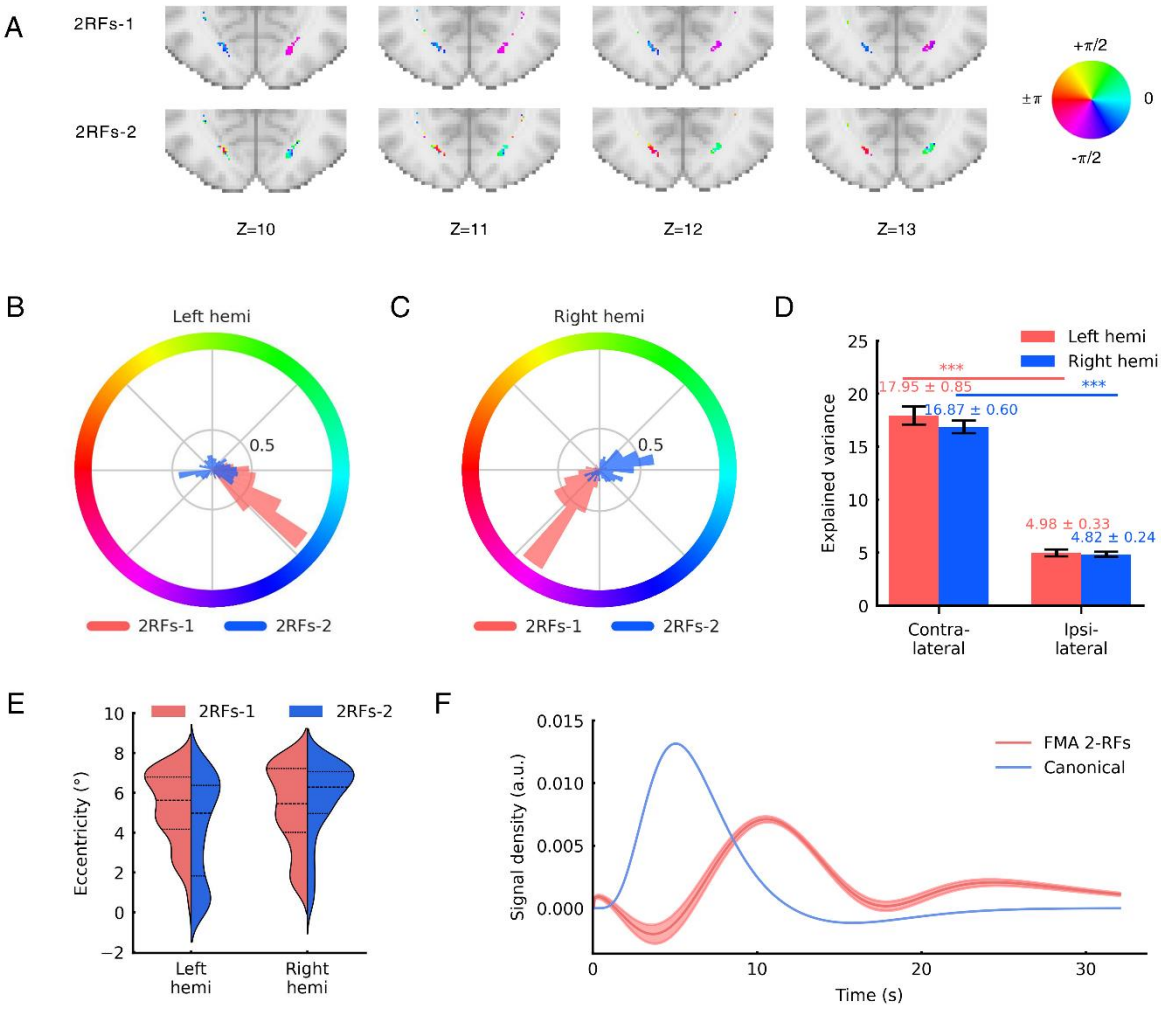

Fig. S5. **Polar angle distribution, visual field map properties and hemodynamic response functions (HRFs) in dual population receptive field (pRF) model winning voxels.** (A) Polar angle distribution maps from pRF estimation for dual receptive fields. The first row corresponds to pRF-1, and the second row to pRF-2 in the model. slice position is indicated by the *z*-coordinate in Montreal Neurological Institute (MNI) space (in millimeters). (B) Comparison of explained variance(%) between contralateral and ipsilateral voxels in the left and right hemispheres (C), D) Normalized polar angle rectangular distribution maps for dual receptive fields in the left and right hemispheres, respectively;. shaded area indicate overlapping angular ranges between pRF-1 and pRF-2. (E) Violin plots showing eccentricity distributions (in degrees of visual angle) in the left and right hemispheres for dual pRFs. Black dashed lines indicate the quartile boundaries in the violin plots.(F) Fitted HRF curves. Solid lines represent the mean HRF curve across voxels, and shaded areas represent bootstrapped 95% confidence intervals.

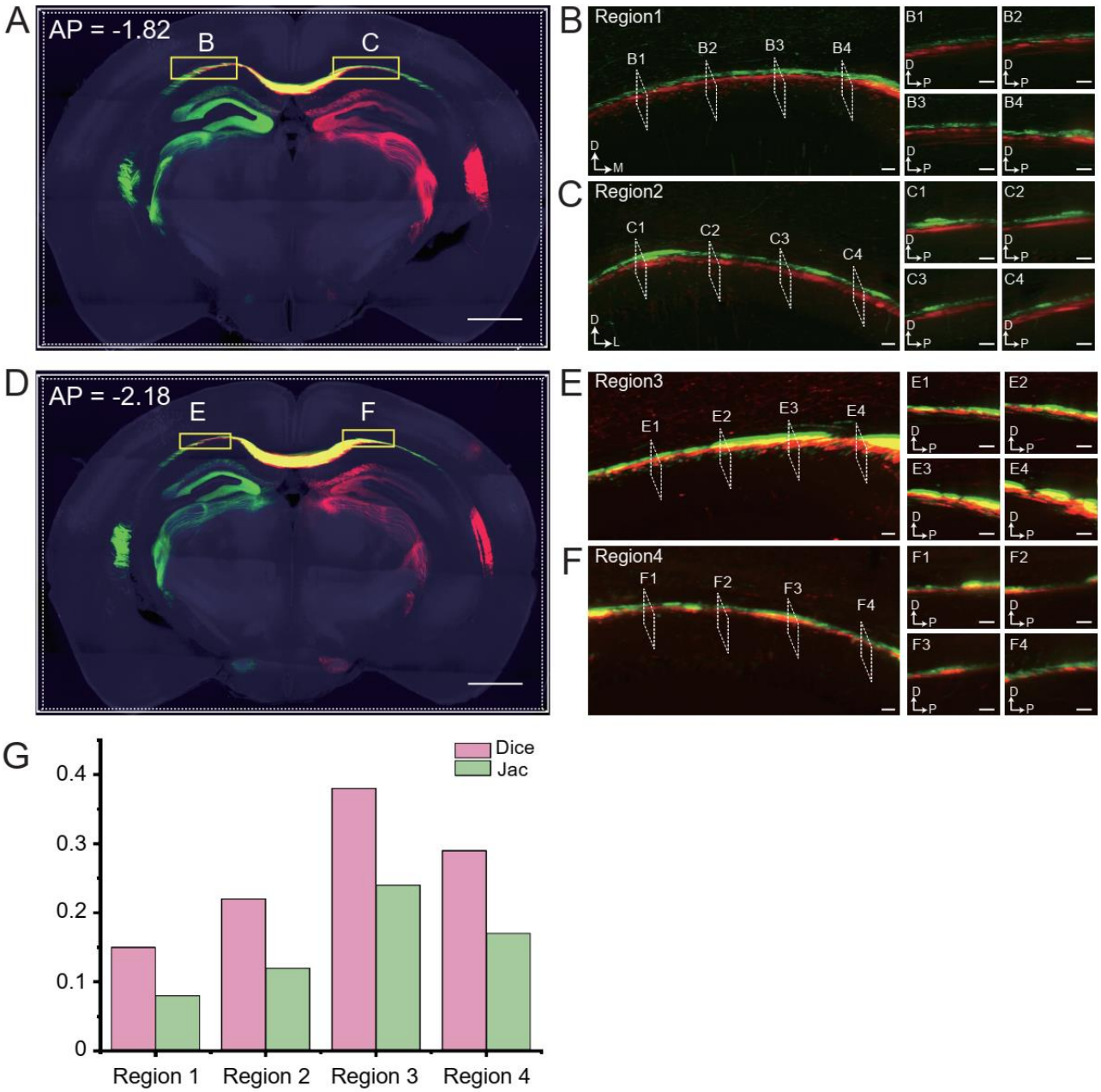

Fig. S6. **Spatial segregation of hemisphere-specific fiber bundles in the mouse corpus callosum.** (A&D) Maximum intensity projections of a 300-μm-thick coronal brain slices showing primary visual cortex projection. (B&C) Structural features of the corpus callosum with ROIs outlined in yellow in (A); (B1-B4) and (C1-C4) Representative sagittal sections through the corresponding ROIs along the medial-lateral axis, spaced at 200 μm intervals. (E&F) Structural features of the corpus callosum with ROIs outlined in yellow in (D); (E1-E4) and (F1-F4) Representative sagittal sections through the corresponding ROIs along the medial-lateral axis, spaced at 200 μm intervals. (G) Spatial overlap of the two fluorescently labeled fiber populations quantified by the Dice coefficient and Jaccard index.